Silver route to cuprate analogs

Jakub Gawraczyński[a,b], Dominik Kurzydłowski[a,c], Russell A. Ewings[d], Subrahmanyam Bandaru[a], Wojciech Gadomski[b], Zoran Mazej[e], Giampiero Ruani[f], Ilaria Bergenti[f], Tomasz Jaroń[a], Andrew Ozarowski[g], Stephen Hill[g,h], Piotr J. Leszczyński[a], Kamil Tokár[i,j], Mariana Derzsi[a,j], Paolo Barone[k], Krzysztof Wohlfeld[l], José Lorenzana[m,1], and Wojciech Grochala[a,1]

[a]Center of New Technologies, University of Warsaw, 02089 Warsaw, Poland; [b]Faculty of Chemistry, University of Warsaw, 02093 Warsaw, Poland; [c]Faculty of Mathematics and Natural Sciences, Cardinal Stefan Wyszyński University in Warsaw, 01938 Warsaw, Poland; [d]ISIS Facility, Science and Technology Facilities Council Rutherford Appleton Laboratory, Didcot OX11 0QX, United Kingdom; [e]Department of Inorganic Chemistry and Technology, Jožef Stefan Institute, SI-1000 Ljubljana, Slovenia; [f]Institute of Nanostructured Materials (ISMN), Consiglio Nazionale delle Ricerche, 40129 Bologna, Italy; [g]National High Magnetic Field Laboratory, Florida State University, Tallahassee, FL 32310; [h]Department of Physics, Florida State University, Tallahassee, FL 32306; [i]Institute of Physics, Slovak Academy of Sciences, 845 11 Bratislava, Slovakia; [j]Advanced Technologies Research Institute, Faculty of Materials Science and Technology in Trnava, Slovak University of Technology in Bratislava, 917 24 Trnava, Slovakia; [k]Superconducting and Other Innovative Materials and Devices Institute (SPIN), Consiglio Nazionale delle Ricerche, 66100 Chieti, Italy; [l]Faculty of Physics, University of Warsaw, 02093 Warsaw, Poland; and [m]Institute for Complex Systems (ISC), Consiglio Nazionale delle Ricerche, Dipartimento di Fisica, Università di Roma "La Sapienza," 00185 Rome, Italy

Edited by Zachary Fisk, University of California, Irvine, CA, and approved December 12, 2018 (received for review July 26, 2018)

The parent compound of high-T_c superconducting cuprates is a unique Mott insulator consisting of layers of spin-1/2 ions forming a square lattice and with a record high in-plane antiferromagnetic coupling. Compounds with similar characteristics have long been searched for without success. Here, we use a combination of experimental and theoretical tools to show that commercial AgF_2 is an excellent cuprate analog with remarkably similar electronic parameters to La_2CuO_4 but larger buckling of planes. Two-magnon Raman scattering and inelastic neutron scattering reveal a superexchange constant reaching 70% of that of a typical cuprate. We argue that structures that reduce or eliminate the buckling of the AgF_2 planes could have an antiferromagnetic coupling that matches or surpasses the cuprates.

silver fluorides | superconductivity | cuprates | strong correlation | quantum magnetism

Cuprates are said to be unique materials in that they combine low-dimensional arrangements of spin-1/2 magnetic moments coupled by a record high antiferromagnetic interaction, strong covalence between transition metal (TM) and ligands, and no orbital degeneracy. The strong quantum nature of spin-1/2 ions manifests itself in several properties. Materials with a quasi-1D electronic structure and layered materials show heat transport by magnetic excitations in insulators that rivals that of metals (1, 2). In quasi-1D compounds, magnon excitations are not stable, leading to exotic phenomena, such as spin charge separation (3, 4). Insulating two-leg ladder compounds show a spin-gapped ground state and can become superconducting with pressure and doping (5). Even for insulating layered materials, the magnetic excitation spectrum is remarkably different from the predictions of spin wave theory (6–8). This extreme quantum nature of the magnetism is believed to be at the heart of the high-T_c superconductivity of the doped layered materials (9).

There have been several attempts to replicate the quantum magnetism of cuprates with different TM ions (10). One proposal has been to use nickel(I) in place of copper(II) (11, 12). While $LaNiO_2$ is isoelectronic and isostructural with the infinite-layer parent cuprates, it lacks the strong covalent character between the TM and ligand (13), and antiferromagnetic order has not been found (14, 15). Sr_2IrO_4 has many similarities with cuprates, including a robust antiferromagnetic order of spin-1/2 pseudospins. However, the correlated insulator character is much weaker, and spin–orbit coupling effects dominate (16, 17).

Another obvious possibility is to move down the periodic table from copper to silver (Fig. 1). The electronic structure of silver oxides was explored in the early times of high T_c (18). However, the second ionization potential of silver is nearly 1.2 eV larger than the one of Cu. Therefore, for a compound like AgO (which is formally d^9), it is convenient to transfer electrons from the filled oxygen shells to the TM (Fig. 1*B*). Thus, AgO shows no magnetic ordering as opposed to the formally isoelectronic CuO (Fig. 1*A*). The larger ionization energy of silver can be compensated for by a right step in the periodic table, replacing oxygen with the more electronegative fluorine (Fig. 1*C*).

Fluoroargentates were scrutinized some years ago (19, 20). Cs_2AgF_4 is structurally similar and isoelectronic with La_2CuO_4 (the so-called "214" family). However, alternating orbital ordering stabilized by small structural distortions leads to ferromagnetic intrasheet interactions instead of the robust antiferromagnetic order of cuprates (21–23). Large superexchange constants have been predicted in many fluorargentates (24), and static susceptibility measurements in a quasi-1D system suggest a superexchange constant of the order of that found in the cuprates (25). However, direct access to excitation energies from spectroscopy has not been available to date.

A bonus property of F^- in place of O^{2-} is that, unlike CuO_2 planes, neutral AgF_2 planes are possible, and therefore, the

Significance

Antiferromagnets can host strong quantum fluctuations in their ground state if they combine both low dimensionality and low spin. Materials based on copper oxides (spin-1/2 ions in layered or 1D structures) are unique in optimizing the tendency to strong quantum fluctuations. As a bonus, they show extremely large magnetic interactions, which lead to interesting quantum effects at relatively high temperatures as anomalous transport properties and high-T_c superconductivity in doped systems. Obtaining similar features with other ions has been a long-standing goal. We show that silver and fluorine (which are next to copper and oxygen in the periodic table) in the commercial compound AgF_2 reach the goal, paving the way for a different generation of quantum materials.

Author contributions: J.L. and W. Grochala designed research; W. Grochala conceived research; J.L. and W. Grochala supervised research; J.G., D.K., R.A.E., S.B., W. Gadomski, Z.M., G.R., I.B., T.J., A.O., S.H., P.J.L., K.T., M.D., P.B., K.W., J.L., and W. Grochala performed research; Z.M. contributed new reagents/analytic tools; D.K., R.A.E., A.O., S.H., M.D., P.B., J.L., and W. Grochala analyzed data; and J.L. and W. Grochala wrote the paper.

The authors declare no conflict of interest.

This article is a PNAS Direct Submission.

[1]To whom correspondence may be addressed. Email: jose.lorenzana@cnr.it or w.grochala@cent.uw.edu.pl.

This article contains supporting information online at www.pnas.org/lookup/suppl/doi:10.1073/pnas.1812857116/-/DCSupplemental.

Published online January 16, 2019.

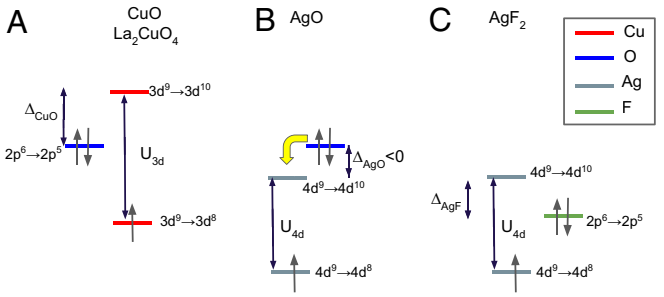

Fig. 1. Schematic energy levels of cuprates and argentates in an ionic picture. All levels are assumed to be referenced to a common zero energy vacuum so that the $3d^9 \rightarrow 3d^{10}$ ($4d^9 \rightarrow 4d^{10}$) level is located at minus the second ionization energy of Cu (Ag). (*A*) Levels for CuO and La_2CuO_4. Cu is in the d^9 configuration. Electron addition ($3d^9 \rightarrow 3d^{10}$) and removal ($3d^9 \rightarrow 3d^8$) energies from Cu correspond to the centroid of the upper and lower Hubbard bands, while removal from filled oxygen corresponds to the valence band. The charge transfer energy Δ_{CuO} and the Hubbard U_{3d} parameter are indicated. (*B*) In the case of AgO, silver is formally d^9. However, since the $4d^9 \rightarrow 4d^{10}$ levels are deeper than the 3*d* counterpart, the charge transfer energy is practically zero or even negative, and the pictured filling is unstable toward more complex mixed valence behavior (yellow arrow) (18). (*C*) Fluorine is more electronegative than O, which translates into deeper $2p^6$ removal states and restores a positive charge transfer energy in AgF_2.

simplest compound is not of the 214 kind but is simply 012. Unexpectedly, as we show here, the binary and commercially available AgF_2 compound turns out to be an excellent cuprate analog. Fig. 2 *A* and *B* and *SI Appendix*, Fig. S1 show the structure (26) and stacking of planes in AgF_2. The topology is the same as in La_2CuO_4, which in the low-temperature orthorhombic (LTO) phase, also has the same pattern of displacements of the ligands out of the plane (+ or −) but with a much smaller magnitude. Also, as in parent cuprates, the ground state of AgF_2 is antiferromagnetic (26) with a staggered moment of 0.7 μ_B (0.6 μ_B), a weak ferromagnetic component of $1 \times 10^{-2} \mu_B$ ($2 \times 10^{-3} \mu_B$) per TM ion, and a Néel temperature of 163 K (325 K), where parentheses enclose reference values (27) in La_2CuO_4.

Results

Density functional theory (DFT) computations show that the electronic structure of AgF_2 is very similar to that in cuprates. Fig. 2*C* shows hybrid DFT calculations comparing the characters of the density of states (28). Both compounds have well-separated Hubbard bands of dominant $d_{x^2-y^2}$ character (indicated by red arrows in Fig. 2*C*), while the first ionization states are of dominant p character; therefore, both compounds are predicted to be charge transfer insulators according to the classification scheme of Zaanen et al. (29). The small charge transfer gap is considered a key characteristic of cuprates. Our unbiased computations in Fig. 2*C* predict that AgF_2 should have an even smaller charge transfer energy than the cuprates, which can provide a test platform for theories based on the smallness of this parameter (30).

As a minimal model of the electronic structure, we consider one $d_{x^2-y^2}$ orbital centered on the TM [as in cuprates (31)] and two p orbitals on the F sites (one more than the cuprates). $p_\parallel$ indicates the p orbital parallel to the TM–TM bond, while p_z is perpendicular to the bond but also mixes with the $d_{x^2-y^2}$ orbitals because of the substantial buckling (*SI Appendix*, *SI Text* and Fig. S2). From unpolarized DFT computations, we find that the hopping integral of a hypothetically straight Ag–F–Ag bond with the same interatomic distances is $t_{pd} = 1.38$ eV, practically the same value as the cuprates (32) (*SI Appendix*, *SI Text* and Figs. S3 and S4). However, due to the increased corrugation of the planes and the destructive interference of the $p_\parallel$ and p_z orbitals, the effective hybridization is smaller, which explains the narrower upper Hubbard band of AgF_2 in Fig. 2*C* (*SI Appendix*, Table S1).

The similar splitting between Hubbard bands shown in Fig. 2*C* for AgF_2 and La_2CuO_4 (9.4 and 10.7 eV, respectively) suggests that the Hubbard U_d parametrizing the Coulomb repulsion on the $d_{x^2-y^2}$ orbitals is similar in the two compounds. However, this estimate does not properly take into account the polarizability of the environment. An empirical estimate of U_d can be obtained from Auger experiments in compounds with similar ions but a filled d shell. Thus, for Cu_2O (Cu d^{10}), Sawatzky and coworkers (33) obtained $U_{3d} = 9.2$ eV, which is close to the accepted value for Cu d^9 in CuO_2 planes. For Ag_2O (Ag d^{10}), they obtained $U_{4d} = 5.8$ eV, which is smaller than for $3d$, which is expected for the more diffuse $4d$ orbitals but still quite large. This value, however, cannot be directly transposed to AgF_2, because the difference in screening has to be taken into account. Screening of the free ion Hubbard U_0 to the value U in the solid is determined by the relaxation energy R of the environment according to $U = U_0 - R$. For TM compounds, R is expected to scale with the polarization of the ligands and to be inversely proportional to the ligand–TM distance to the fourth power (34). For copper oxides, typical values of the oxygen polarizability are in the range $\alpha_O = 1.9 \sim 3.2$ Å^3. Instead, in

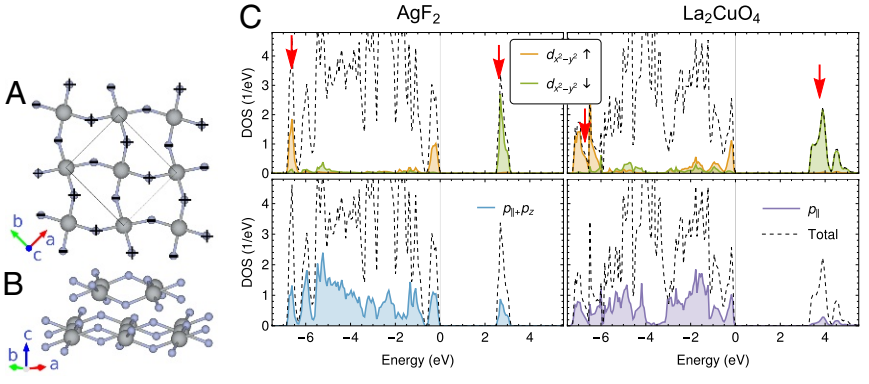

Fig. 2. AgF_2 vs. La_2CuO_4. (*A*) Top view of a plane in AgF_2. The black rectangle indicates the unit cell. Big/small atoms are Ag/F. We indicate the sign of F displacements in the *c* direction. Notice that nearest neighbor exchange paths are equivalent, although the overall symmetry is orthorhombic as in the LTO phase of La_2CuO_4. (*B*) Side view showing buckling and stacking of planes. (*C*) Comparison of the orbital resolved (*Upper*: $d_{x^2-y^2}$; *Lower*: $p_\parallel$ and p_z) and total (dashed lines) density of states of the two compounds computed within hybrid DFT in the antiferromagnetic state. The red arrows indicate the Hubbard bands.

AgF_2, the ligand–TM distance is larger, and the polarizability of the ligand is much smaller at $\alpha_F = 0.64$ Å^3, leading to less efficient screening. This allows for values of U_d in AgF_2 similar to the cuprates (*SI Appendix*, *SI Text*). Interestingly, from a different perspective, the computations of Fig. 2*C* suggest the same conclusion.

The similarity of the DFT electronic structures confirms the conclusions of the simplistic picture of Fig. 1 *A* and *C*. From the point of view of the strength of the correlation, the narrower upper Hubbard band of AgF_2 suggests a more correlated system but a smaller U_d and smaller charge transfer gap point in the opposite direction. Our results imply that AgF_2 is very covalent, probably more so than the cuprates, which is consistent with core- and valence-level spectroscopy results (35) but in contrast with the prevailing view that fluorides are ionic compounds.

The more interesting parameter for a cuprate analogue is the magnetic exchange interaction, which determines the scale of magnetic fluctuations in magnetically mediated mechanisms of superconductivity in doped compounds. Not surprisingly, AgF_2 is antiferromagnetic (26) as predicted by Anderson superexchange.

A perturbation theory analysis shows that the dominant interaction is antiferromagnetic due to processes in which two holes from neighboring Ag sites occupy simultaneously the bridging F (*SI Appendix*, *SI Text*). As in cuprates (36), one needs to also consider processes in which two holes occupy the same Ag site (also antiferromagnetic) and direct ferromagnetic exchange. Buckling tends to reduce the antiferromagnetic contribution as $\cos^2(\eta)$, where $\eta = 132.4^\circ$ is the Ag–F–Ag angle (*SI Appendix*, Eq. **S8**). While model computations have been very useful to discuss the dependence of the magnetic interaction in fluroargentates on the structure (37), the present lack of precise parameters does not allow one to obtain an accurate absolute value. An alternative estimate can be obtained from hybrid DFT computations, which yield $J = 56$ meV for the nearest neighbor interaction (Table 1) (24). Computations (37) done with a new generation functional (38) yield $J = 71$ meV.

As in La_2CuO_4, the TM in one plane coincides with the center of the four-TM plaquette in the next plane, which tends to frustrate interplanar magnetic interactions in an antiferromagnetically ordered state. In both compounds, the frustration is partially relieved by the orthorhombicity, but the effect is much larger in AgF_2. For the ratio of interlayer to intralayer couplings, our DFT computations predict values of the order of 10^{-2} (*SI Appendix*, Table S2), a larger ratio than the experimental (27) one in cuprates (10^{-5}) but still well in the regime of a quasi-2D quantum antiferromagnet.

Table 1. Exchange constants for AgF_2 and its two hypothetical polymorphs

Polymorph	Cell vectors (Å)			R (Å)	η	J (meV)
	a	b	c			
$\alpha - AgF_2$	5.191 (5.101)	5.662 (5.101)	6.042 (5.831)	4.198	132.4	56 (70)
$\delta - AgF_2$	5.671	5.670	5.607	4.166	148.5	137
$\omega - AgF_2$	5.836	5.836	6.213	4.127	180	195

We report key structural parameters and values of the nearest neighbor magnetic coupling constant calculated with the DFT total energy method. R is the sum of the two Ag–F distances of the bond. $\alpha - AgF_2$ is the known stable phase in which experiments have been done (experimental values are given in parentheses). $\omega - AgF_2$ is tetragonal, but cell parameters are reported in the $\sqrt{2} \times \sqrt{2} \times 1$ unit cell for comparison. The text has a detailed description of the polymorphs. A hybrid functional was used (*Materials and Methods*). Notice that this functional yields a value of J below experiment. After this work was finished, a more accurate value was obtained in ref. 37.

We used a full set of exchange constants with longer-range interactions (*SI Appendix*, Table S2) from DFT computations to estimate the Néel temperature with classical Monte Carlo computations (*SI Appendix*, *SI Text*). Correcting approximately for quantum effects, we found a value higher than the experimental one (by 27%) but of the same order. Given the approximations involved, this fair agreement validates the hybrid DFT computations of exchange constants. As shown below, Raman experiments reveal an even larger value of the effective nearest neighbor exchange. We believe that uncertainties in the interplanar coupling and extra terms in the Hamiltonian, like four-site cyclic exchange, can explain the mild difference between the DFT + Monte Carlo estimate of the Néel temperature and the experiment.

To further test the analogy, we experimentally studied high-quality powder samples of freshly prepared AgF_2. Crystallinity was verified with powder X-ray diffraction, which resulted in a spectrum with similar characteristics but fewer impurity signatures than a commercial sample (*SI Appendix*, *SI Text* and Fig. S5).

Specific heat measurements reveal that only about 5% of the maximum possible entropy change $R\ln(2)$ occurs around the Neél temperature (*SI Appendix*, *SI Text* and Fig. S6). This is consistent with a quasi-2D antiferromagnet, where short-range in-plane correlations set in at much higher temperatures than the 3D Néel temperature. A bulk EPR signal was searched over a wide range of temperatures. However, despite several efforts, it was not found. This is also analogous to the situation in the cuprates and points to strong antiferromagnetic interactions (*SI Appendix*, *SI Text*). Vibrational spectroscopy (Raman and IR) shows phonon modes in good agreement with the prediction of hybrid DFT, validating the latter computations (*SI Appendix*, Fig. S7). In addition, the detailed phonon assignment (*SI Appendix*, *SI Text* and Table S3) allowed us to check the integrity of the sample under the laser spot and to exclude impurity phases or photochemistry by-products.

For high Raman shifts, we detected a broad band centered at 1,750 cm^{-1} at room temperature, which hardens and becomes narrower on cooling (Fig. 3*A*). The temperature dependence is very similar to the one for two-magnon Raman scattering in cuprates (39). This allows us to identify unambiguously this line as due to two-magnon Raman scattering in AgF_2. Comparing with cuprates, we deduce that the antiferromagnetic exchange in this compound is $J_{AF} = 70$ meV, confirming the expected large antiferromagnetic interaction and in excellent agreement with the computation of ref. 37. The robustness of two-magnon Raman scattering well above the Néel temperature also confirms strong short-range antiferromagentic correlations, also like in cuprates.

Fig. 3*B* shows the two-magnon Raman line recorded with three different apparatuses (*Materials and Methods*). The line shape is clearly visible with excitation energies of 1.17 and 1.58 eV. The feature at 970 cm^{-1} is assigned to a two-phonon process. For 2.41 eV, the two-magnon feature is weak at high temperature (compared with the two-phonon feature) but becomes stronger on cooling, similar to the behavior for 1.17 eV (Fig. 3*A*) and for cuprates. Unfortunately, a detailed line shape analysis is not possible in this case due to a strong energy-dependent background (dashed lines in Fig. 3*B*). The dependence on the excitation energy suggests that the resonance profile of the two-magnon line is shifted to lower laser excitation energies with respect to what is found in cuprates (40), which is consistent with the smaller charge transfer gap found in DFT.

To confirm the large value of J, we performed inelastic neutron scattering experiments in a 150-g AgF_2 powder sample. The experimental excitation spectrum (Fig. 4*A* and *SI Appendix*, Fig. S8*A*) shows a plume (indicated by the arrow in Fig. 4*A*) at a value of $|\mathbf{Q}|$ corresponding to the propagation vector of the

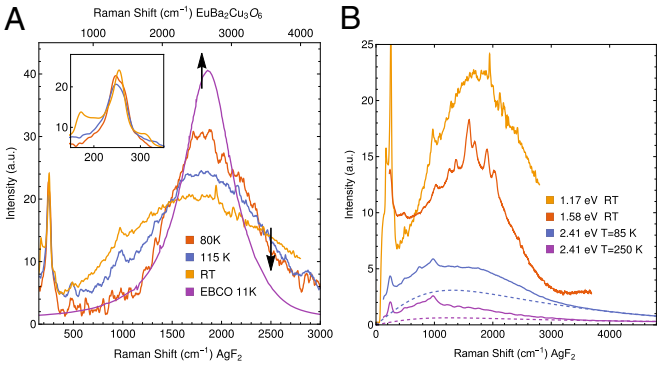

Fig. 3. Two-magnon Raman spectra of AgF_2. (*A*) Temperature dependence for excitation energy 1.17 eV. We also show the low-temperature two-magnon line shape of $EuBa_2Cu_3O_6$ (EBCO) after ref. 39. The upper scale corresponds to EBCO, while the lower scale corresponds to AgF_2 (this work). Curves are labeled by the temperature in Kelvin. Comparing the energy scales in *A*, we obtain that $J_{AF} = 0.7J_{EBCO}$, which yields $J_{AF} = 70$ meV for AgF_2. A linear background was subtracted to the spectra at 80 and 115 K but not to the room temperature spectrum, which was measured using a different machine (*Materials and Methods*). Spectra at different temperatures/apparatus were normalized with the phonon lines as shown in *Inset*. (*B*) We show data for AgF_2 at various excitation energies. For the 2.41-eV laser line, two temperatures are reported. Dashed lines are estimated nonmagnetic backgrounds, which are well defined at high energy but cannot be uniquely defined at low energy.

magnetic order, $\mathbf{Q}_{\mathrm{AF}}$. The plume originates on the powder average of the acoustic spin wave excitations emanating from $\mathbf{Q}_{\mathrm{AF}}$ (i.e., the Goldstone mode) and is typical of steep dispersions (41) consistent with a large value of J. Fig. 4*B* is a simulation using spin wave theory (42). Although the plume is well explained by the theory using an in-plane magnetic exchange constant similar to the one in Raman, uncertainty in the data allows for considerable freedom on the admissible values of J. The situation is different for the flat band at 148 $\pm$3 meV. Simulations show that this flat band originates in the maximum of the magnetic dispersion relation, which produces a Van Hove-like singularity when averaged over all possible grain orientations in our powder sample, and its energy is roughly $2J$ (plus small corrections due to interplanar coupling). The sensitivity to the in-plane exchange allows to confirm $J = 70$ meV as found in Raman.

The intensity of the flat band has an interesting dependence on wave vector, which is determined by the magnetic form factor. Unfortunately, the atomic form factor of Ag in the d^9 configuration is not available in the standard sources (43). Using instead a Pd d^9 form factor (as the closest available $4d$ anion with a known atomic form factor), we find a flat band intensity, which is peaked at much smaller wave vectors respect to experiment (*SI Appendix*, Fig. S8*B*). In the simulation in Fig. 4*B*, we used a DFT form factor computed as in ref. 44, which substantially improves the agreement with respect to the atomic form factor but still yields a maximum of intensity at around 5 Å^{-1} instead of the maximum near 8 Å^{-1} observed in the experiment. Strong covalency of the Ag–F bond is essential for the improvement in the DFT simulation with respect to the atomic form factor. We attribute the differences still observed to the known deficiencies of DFT to accurately describe the bond charges in a correlated material (45).

Discussion

The above results clearly indicate that AgF_2 is an excellent cuprate analog with a very similar electronic structure and large magnetic interaction. Putting AgF_2 under high pressure does not flatten but tends to form lower-dimensional structures (46). Remarkably, it has been predicted that the observed structures as a function of pressure should lead to quasi-1D magnetism and ladders with extremely high antiferromagnetic constants, allowing one to visit practically all of the physics of low-dimensional quantum magnets in the same compound (37).

Historically, the superconducting temperature in cuprates has been optimized starting from simple ternary compounds and increasing the number of chemical elements. In argentates, starting from a binary compound that is already stable leaves substantial freedom for such optimizations.

Clearly, a high priority is to produce doped AgF_2 planes. One concern (47) is that ionic distortions may self-trap carriers and hinder metallic conduction and superconductivity. Similar to ref. 48, we computed lattice spin polarons using DFT + U (*Materials and Methods*). For electron-doped AgF_2, we find that polaronic tendencies are very strong and that electrons self-trap. For the hole-doped case, polaronic tendencies are stronger than cuprates due to the large buckling but remain moderate. Indeed, the energy gain due to lattice relaxation is smaller than the estimated bandwidth and of the order of the breathing phonon frequency ($\sim$60 meV), indicating that metallic conduction may still be possible if high-enough doping is achieved. Polaronic tendencies should be further reduced in the case of the flat-layer polymorphs discussed below.

The cuprate family of parent high-T_c superconductors is made of materials very similar to each other. Indeed, changes in key parameters, like J, are smaller than 15% (49). This severely hampers the identification of clear trends in physical properties. A close cuprate analog but with important differences (less marked 2D character, smaller J, narrower bands, smaller charge transfer gap, rich polymorphism) opens the way to the clarification of the mysterious cuprate-phase diagram by revealing clear trends.

Another desirable development is to make the planes flat, which according to *SI Appendix*, Eq. **S8**, should increase J. Such hypothetical polymorphs were studied in the past with DFT (20, 50–53). One such structure (20, 51) dubbed $\delta - AgF_2$ is obtained by constraining the AgF_2 plane to be a mirror plane but allowing the Ag–F–Ag bond to have an angle inside the plane. This polymorph shows a modest increase in energy at ambient pressure with a large value of J according to DFT computations (20). Since this kind of functional may overestimate the magnetic

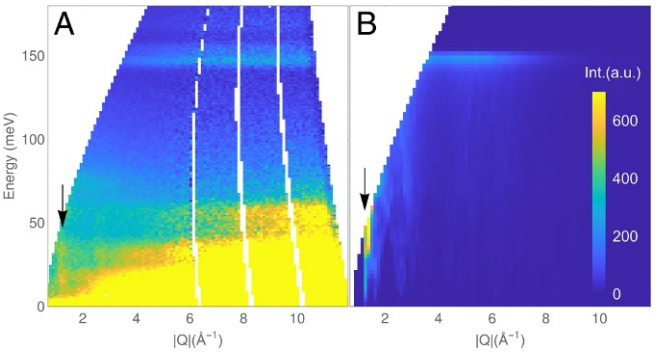

Fig. 4. Powder inelastic neutron scattering. (*A*) Measured neutron scattering cross-section taken with incident neutron energy (E_i) of 300 meV. The vertical plume of scattering indicated by the arrow corresponds to $|\mathbf{Q}| \approx 1.2$ Å^{-1}, where $\mathbf{Q}$ is the propagation vector of the magnetic order [(1,0,0) in reciprocal lattice units]. The strong signal at high $|\mathbf{Q}|$ extending up to 60 meV corresponds to scattering from phonons, and the strong $|\mathbf{Q}|$-independent signal at very low energy corresponds to incoherent elastic scattering. (*B*) Calculation of a powder-averaged neutron scattering cross-section using spin wave theory, performing a powder average, and convoluting with the instrumental resolution. We used an intraplanar value of $J = 70$ meV and interplanar $J_\perp = 4$ meV as suggested by the DFT computations (*SI Appendix*, Table S2).

interaction, we have repeated the computation with hybrid DFT, which yields a value of 137 meV as shown in Table 1. If one further restricts the bond angles to be straight, a tetragonal polymorph is obtained (52) dubbed $\omega - AgF_2$. In this case, a nearest neighbor exchange approaching 200 meV is obtained. Obviously, such polymorphs are not stable at ambient pressure. However, it is possible that they can be stabilized by intercalation or that they may be grown as one or few layers on an appropriate substrate. Generally, we find that flat AgF_2 planes should have an antiferromagnetic J, which is more than twice the one of commercial AgF_2 and assuming a magnetically driven mechanism (54), could potentially lead to superconducting critical temperatures higher than those exhibited by cuprates.

Materials and Methods

Structure. Visualization of the structure was performed with the use of the VESTA software (55). The crystal structure of AgF_2 has been described in detail before based on powder neutron data (56–58). At ambient conditions, AgF_2 crystallizes in a distorted rutile-type structure of orthorhombic symmetry. This structure contains puckered AgF_2 sheets containing corner-sharing AgF_4 plaquettes. The octahedral coordination of Ag^{2+} is completed by two fluorine atoms from neighboring sheets. This structure can thus be described as built of puckered 2D sheets. *SI Appendix*, Fig. S1 compares the structure of AgF_2 with a typical cuprate.

DFT Computations. Unpolarized DFT calculations have been performed using the projector-augmented waves method as implemented in VASP (59) within the generalized gradient approximation of Perdew et al. (60) (PBE) and the crystal structure of ref. 26. The band structure was obtained for the experimental lattice (26) using a Monkhorst–Pack mesh of 26 ×26× 26 k points and a 500-eV plane wave cutoff. A smaller mesh of 8 ×8× 8 k points has been used for the projection onto maximally localized Wannier functions. Polarized computations where done with the HSE06 functional (61), which is a hybrid functional mixing PBE with 25% of Hartree–Fock exchange energy.

For the phonon assignments, dynamical matrix interatomic force constants and polarizabilities (macroscopic dielectric tensors) for computing IR and Raman intensities were obtained from the density functional perturbation theory scheme with (6 × 6 × 7) k-point mesh (including 64 irreducible points) and cutoff = 520 eV using PBEsol functional in combination with Hubbard U for Ag^{2+} ions with one unpaired electron (electronic configuration $3d^9$) within the DFT + U scheme as implemented in the VASP package (59). The Hubbard U_{Ag} (23) was set to 5 eV, and J_H was set to 1 eV.

The Γ-point vibrational frequencies were calculated by diagonalizing the dynamical matrix for the fully converged structural AgF_2 model. IR intensity of vibrational eigenmodes has been expressed within dipole approximation in terms of atom-born effective charges and corresponding phonon eigenvectors using the formula for modal oscillator strengths (62, 63) as implemented in ref. 64. Intensity of each Raman mode was calculated as implemented in ref. 65. The electronic and ionic convergence was restricted to 10^{-8} and 10^{-7} eV, respectively. The atomic forces were converged to a maximal value of 0.02 meV/Å. For the polaron configurations, we added or removed one electron from a $\sqrt{2} \times \sqrt{2} \times 1$ supercell corresponding to 1/8 doping.

Raman Scattering. Raman spectra shown in Fig. 3 and *SI Appendix*, Fig. S7 were acquired on a dry quartz capillary filled with AgF_2 in the 180° scattering geometry. The capillary was prefluorinated with F_2 gas to minimize reactivity toward AgF_2. Using larger power than the ones reported may lead to decomposition of the samples. Data were taken in the following instruments: (*i*) Nicolet 6700/NXR FT-Raman equipped with an Nd:YAG laser for excitation at 1,064 nm (1.17 eV), a Nicolet reflective mirror, and a liquid nitrogen cooled Ge detector. Spectra were acquired with resolution of 4 cm^{-1} at 4–5 mW of laser power and referenced to that of elemental silicon. Calibration was done with respect to a standardized built-in Xe lamp. A typical measurement was composed of several thousand accumulations (of ∼2 s each) and took several hours to complete. This configuration has high sensitivity and was used for the weak two-magnon feature at room temperature. (*ii*) Low-temperature measurements at identical source/detector combination as in *i* were done in an RFS 100 Bruker Raman interferometer with a resolution of 4 cm^{-1}. This instrument was calibrated with a black body source at 1,273 K placed in the sample position. The incident laser power density was set at 1.1 W/cm^2 (80 mW, ∼3-mm laser beam diameter). The sample was mounted on the cold finger of a liquid He flow cryostat. Each spectrum is the average of 4,000 or 16,000 scans (2 or 8 h). (*iii*) A T64000 spectrometer from Horiba–Jobin Yvon equipped with a liquid nitrogen cooled Si detector and used in the confocal microscope mode (aperture diameter: 150 μm) with the Mitutoyo long-working distance lenses (focal length of 200 mm). Typical gratings used were 150 lines per millimeter (preliminary monochromatization stage) and 300 lines per millimeter (second monochromatization stage). Calibration was done with a black body source at 1,200 °C placed in the sample position. The 514.5-nm (2.41 eV, 420 mW at head) Kr/Ar gas ion laser from Spectra-Physics was used as a source. Spectra were acquired with resolution of 4.5 cm^{-1} or better at maximum 5 mW of laser power on the cell and referenced to that of diamond or silicon. Filters were used to bring down the beam power at the sample (in some cases, down to 0.4 mW). A typical measurement was composed of 340 accumulations (60 s each). (*iv*) Renishaw inVia Raman system with a 785-nm (1.58-eV) line used as the excitation source. The light from the laser was passed through a line filter and focused on the sample mounted on an *x–y–z* translation stage with a 50× microscope objective. The Raman-scattered light was collected by the same objective through a holographic notch filter to block out Rayleigh scattering. The microscope was equipped with an 1,800-grooves per millimeter grating, cutoff optical filters, and a 1,024 × 256-pixel Peltier-cooled RenCam CCD detector, which allowed for registering of the Stokes part of Raman spectra with 5- to 6-cm^{-1} spectral resolution and 2-cm^{-1} wavenumber accuracy. Calibration was done with a standardized He/Ne lamp. The time required for completing a single Raman spectrum was 4 min with a laser power of 0.25 mW.

Inelastic Neutron Scattering. Neutron scattering measurements were performed on the MAPS spectrometer at the ISIS pulsed neutron and muon source. A monochromatic neutron beam was selected using a Fermi chopper, spinning at 150 Hz for incident neutron energy (E_i) of 60 meV and 400 Hz for E_i = 300 meV. A sample of 150 g of mass was contained in an annular geometry inside an aluminum can filled with Ar. Details of the simulations are in *SI Appendix, SI Text*.

ACKNOWLEDGMENTS. W. Grochala thanks A. Michota-Kaminska for making the Renishaw inVia Raman system available. Experiments at the ISIS Neutron and Muon Source were supported by a beamtime allocation from the Science and Technology Facilities Council. The high-field EPR spectra were recorded at the National High Magnetic Field Laboratory, which is funded by NSF Cooperative Agreement DMR-1157490 and the State of Florida. Research at the University of Warsaw was carried out with the use of Center for Preclinical Research and Technology (CePT) infrastructure financed by the European Union—the European Regional Development Fund within Operational Program "Innovative Economy" for 2007–2013 POIG.02.02.00-14-024/08-00. The quantum mechanical calculations performed in Warsaw would not have been possible without the Interdisciplinary Centre for Mathematical and Computational Modelling (ICM) supercomputer Okeanos (ADVANCE PLUS, GA67-13). Z.M. acknowledges the Slovenian Research Agency for financial support within Research Program P1-0045 Inorganic Chemistry and Technology. S.H. received financial support through NSF Grant DMR-1610226. J.L. acknowledges support from CINECA High-Performance Computer Project IsC50_HTCM, Italian Foreign Affairs and International Cooperation Ministry (MAECI) Collaborative Projects SUPERTOP-PGR04879 and AR17MO7, and Regione Lazio (L.R. 13/08) Project SIMAP. W. Grochala acknowledges support from Polish National Science Center Maestro Project UMO-2017/26/A/ST5/00570.

1. Hofmann M, et al. (2003) Evidence for a large magnetic heat current in insulating layered cuprates. *Phys Rev B*67:184502.
2. Hess C (2018) Heat transport of low-dimensional quantum magnets. arXiv: 1805.01746.
3. Kim C, et al. (1996) Observation of spin-charge separation in one-dimensional $SrCuO_2$. *Phys Rev Lett* 77:4054–4057.
4. Kim BJ, et al. (2006) Distinct spinon and holon dispersions in photoemission spectral functions from one-dimensional $SrCuO_2$. *Nat Phys* 2:397–401.
5. Dagotto E (1999) Experiments on ladders reveal a complex interplay between a spin-gapped normal state and superconductivity. *Rep Prog Phys* 62:1525–1571.
6. Lorenzana J, Sawatzky GA (1995) Theory of phonon-assisted multimagnon optical absorption and bimagnon states in quantum antiferrromagnets. *Phys Rev B* 52:9576–9589.
7. Ho CM, Muthukumar VN, Ogata M, Anderson PW (2001) Nature of spin excitations in two-dimensional Mott insulators: Undoped cuprates and other materials. *Phys Rev Lett* 86:1626–1629.
8. Christensen NB, et al. (2007) Quantum dynamics and entanglement of spins on a square lattice. *Proc Natl Acad Sci USA* 104:15264–15269.
9. Anderson PW, et al. (2004) The physics behind high-temperature superconducting cuprates: The plain vanilla version of RVB. *J Phys Condens Matter* 16:R755–R769.

10. Norman MR (2016) Materials design for new superconductors. *Rep Prog Phys* 79:074502.
11. Anisimov VI, Bukhvalov D, Rice TM (1999) Electronic structure of possible nickelate analogs to the cuprates. *Phys Rev B* 59:7901–7906.
12. Chaloupka J, Khaliullin G (2008) Orbital order and possible superconductivity in $LaNiO_3/LaMO_3$ superlattices. *Phys Rev Lett* 100:3–6.
13. Lee KW, Pickett WE (2004) Infinite-layer $LaNiO_2$: Ni^{1+} is not Cu^{2+}. *Phys Rev B* 70:1–7.
14. Hayward MA, Green MA, Rosseinsky MJ, Sloan J (1999) Sodium hydride as a powerful reducing agent for topotactic oxide deintercalation: Synthesis and characterization of the nickel(I) oxide $LaNiO_2$. *J Am Chem Soc* 121:8843–8854.
15. Ikeda A, Manabe T, Naito M (2013) Improved conductivity of infinite-layer $LaNiO_2$ thin films by metal organic decomposition. *Phys C Supercond Appl* 495:134–140.
16. Kim BJ, et al. (2008) Novel $J_{eff} = 1/2$ Mott state induced by relativistic spin-orbit coupling in Sr_2IrO_4. *Phys Rev Lett* 101:1–4.
17. Fujiyama S, et al. (2012) Two-dimensional Heisenberg behavior of $J_{eff} = 1/2$ isospins in the paramagnetic state of the spin-orbital Mott insulator Sr_2IrO_4. *Phys Rev Lett* 108:1–5.
18. Tjeng LH, et al. (1990) Electronic structure of Ag_2O. *Phys Rev B* 41:3190–3199.
19. Grochala W, Hoffmann R (2001) Real and hypothetical intermediate-valence AgII/AgIII and AgII/AgI fluoride systems as potential superconductors. *Angew Chem Int Ed* 40:2742–2781.
20. Jaroń T, Grochala W (2008) Prediction of giant antiferromagnetic coupling in exotic fluorides of Ag. *Phys Status Solidi Rapid Res Lett* 2:71–73.
21. McLain SE, et al. (2006) Magnetic behaviour of layered Ag(II) fluorides. *Nat Mater* 5:561–565.
22. Grochala W (2006) Magnetism: Small changes, big consequences. *Nat Mater* 5:513–514.
23. Kasinathan D, Koepernik K, Nitzsche U, Rosner H (2007) Ferromagnetism induced by orbital order in the charge-transfer insulator Cs_2AgF_4: An electronic structure study. *Phys Rev Lett* 99:247210.
24. Kurzydłowski D, Grochala W (2017) Prediction of extremely strong antiferromagnetic superexchange in silver(II) fluorides: Challenging the oxocuprates(II). *Angew Chem Int Ed* 56:10114–10117.
25. Kurzydłowski D, Mazej Z, Jagličić Z, Filinchuk Y, Grochala W (2013) Structural transition and unusually strong antiferromagnetic superexchange coupling in perovskite $KAgF_3$. *Chem Commun* 49:6262–6264.
26. Fischer P, Roult G, Schwarzenbach D (1971) Crystal and magnetic structure of silver difluoride-II. Weak 4d-ferromagnetism of AgF_2. *J Phys Chem Solids* 32:1641–1647.
27. Kastner MA, Birgeneau RJ, Shirane G, Endoh Y (1998) Magnetic, transport, and optical properties of monolayer copper oxides. *Rev Mod Phys* 70:897–928.
28. Mazej Z, Kurzydłowski D, Grochala W (2016) Unique silver(II) fluorides: The emerging electronic and magnetic materials. Photonic and Electronic Properties of Fluoride Materials, eds Tressaud A, Poeppelmeier K (Elsevier, Amsterdam), pp 231–260.
29. Zaanen J, Sawatzky GA, Allen JW (1985) Band gaps and electronic structure of transition-metal compounds. *Phys Rev Lett* 55:418–421.
30. Varma CM (1997) Non-Fermi-liquid states and pairing instability of a general model of copper oxide metals. *Phys Rev B* 55:14554–14580.
31. Emery VJ (1987) Theory of high-Tc superconductivity in oxides. *Phys Rev Lett* 58:2794–2797.
32. McMahan AK, Annett JF, Martin RM (1990) Cuprate parameters from numerical Wannier functions. *Phys Rev B* 42:6268–6282.
33. Ghijsen J, et al. (1988) Electronic structure of Cu_2O and CuO. *Phys Rev B Condens Matter* 38:11322–11330.
34. De Boer DKG, Haas C, Sawatzky GA (1984) Exciton satellites in photoelectron spectra. *Phys Rev B* 29:4401–4419.
35. Grochala W, Egdell RG, Edwards PP, Mazej Z, Žemva B (2003) On the covalency of silver-fluorine bonds in compounds of silver(I), silver(II) and silver(III). *ChemPhysChem* 4:997–1001.
36. Eskes H, Jefferson JH (1993) Superexchange in the cuprates. *Phys Rev B* 48:9788.
37. Kurzydłowski D, et al. (2018) Dramatic enhancement of spin–spin coupling and quenching of magnetic dimensionality in compressed silver difluoride. *Chem Commun* 54:10252–10255.
38. Sun J, Ruzsinszky A, Perdew J (2015) Strongly constrained and appropriately normed semilocal density functional. *Phys Rev Lett* 115:036402.
39. Knoll P, Thomsen C, Cardona M, Murugaraj P (1990) Temperature-dependent lifetime of spin excitations in $RBa_2Cu_3O_6$ (R =Eu, Y). *Phys Rev B* 42:4842–4845.
40. Blumberg G, et al. (1996) Resonant two-magnon Raman scattering in cuprate antiferromagnetic insulators. *Phys Rev B* 53:R11930–R11933.
41. Ewings RA, et al. (2008) High-energy spin excitations in $BaFe_2As_2$ observed by inelastic neutron scattering. *Phys Rev B* 78:220501.
42. Toth S, Lake B (2015) Linear spin wave theory for single-Q incommensurate magnetic structures. *J Phys Condens Matter* 27:166002.
43. Brown J (2003) Magnetic form factors. *Neutron Data Booklet*, eds Dianoux AJ, Lander GH; Institut Laue-Langevin (Old City Publishing Group, Philadelphia), pp 2.5-1–2.5-12.
44. Walters AC, et al. (2009) Effect of covalent bonding on magnetism and the missing neutron intensity in copper oxide compounds. *Nat Phys* 5:867–872.
45. Ying ZJ, et al. (2016) Anomalous scaling and breakdown of conventional density functional theory methods for the description of Mott phenomena and stretched bonds. *Phys Rev B* 94:075154.
46. Grzelak A, et al. (2017) High-pressure behavior of silver fluorides up to 40 GPa. *Inorg Chem* 56:14651–14661.
47. Zaanen J, Littlewood PB (1994) Freezing electronic correlations by polaronic instabilities in doped La_2NiO_4. *Phys Rev B* 50:7222–7225.
48. Anisimov VI, Korotin MA, Zaanen J, Andersen OK (1992) Spin bags, polarons, and impurity potentials in $La_{2-x}Sr_xCuO_4$ from first principles. *Phys Rev Lett* 68:345–348.
49. Tokura Y, et al. (1990) Cu-O network dependence of optical charge-transfer gaps and spin-pair excitations in single-CuO_2-layer compounds. *Phys Rev B* 41: 11657–11660.
50. Grochala W (2006) On similarities and differences of the electronic structure for $Cu(II)/O^{2-}$ and $Ag(II)/F^{1-}$ infinite layer compounds. *Scr Mater* 55:811–814.
51. Romiszewski J, Grochala W, Stolarczyk LZ (2007) Pressure-induced transformations of $Ag^{II}F_2$ —towards an 'infinite layer' *d*9 material. *J Phys Condens Matter* 19:116206.
52. Kurzydłowski D (2013) Fluoroargentates(II) of alkali metals – Synthesis, structure, phase transitions and magnetic properties. PhD thesis (University of Warsaw, Warsaw).
53. Yang X, Su H (2015) Electronic properties of fluoride and half–fluoride superlattices $KZnF_3/KAgF_3$ and $SrTiO_3/KAgF_3$. *Sci Rep* 5:15849.
54. Scalapino DJ (2012) A common thread: The pairing interaction for unconventional superconductors. *Rev Mod Phys* 84:1383–1417.
55. Momma K, Izumi F (2011) VESTA 3 for three-dimensional visualization of crystal, volumetric and morphology data. *J Appl Crystallogr* 44:1272–1276.
56. Charpin P, Plurien P, Meriel P (1970) A neutron diffraction study of crystal and magnetic structure of AgF_2. *Bull Soc Fr Miner Cristal* 93:7–13.
57. Fischer P, Schwarzenbach D, Rietveld H (1971) Crystal and magnetic structure of silver difluoride. *J Phys Chem Solids* 32:543–550.
58. Jesih A, et al. (1990) Einkristalluntersuchungen an AgF_2. *Z Anorg Allg Chem* 588:77–83.
59. Kresse G, Furthmüller J (1996) Efficient iterative schemes for ab initio total-energy calculations using a plane-wave basis set. *Phys Rev B* 54:11169–11186.
60. Perdew JP, Burke K, Ernzerhof M (1996) Generalized gradient approximation made simple. *Phys Rev Lett* 77:3865–3868.
61. Krukau AV, Vydrov OA, Izmaylov AF, Scuseria GE (2006) Influence of the exchange screening parameter on the performance of screened hybrid functionals. *J Chem Phys* 125:224106.
62. Giannozzi P, Baroni S (1994) Vibrational and dielectric properties of C_{60} from density-functional perturbation theory. *J Chem Phys* 100:8537–8539.
63. Esfarjani K, Hashi Y, Onoe J, Takeuchi K, Kawazoe Y (1998) Vibrational modes and IR analysis of neutral photopolymerized C_{60} dimers. *Phys Rev B* 57:223–229.
64. Karhánek D, Bučcko T, Hafner J (2010) A density functional study of the adsorption of methane-thiol on the (111) surfaces of the Ni-group metals. I. Molecular and dissociative adsorption. *J Phys Condens Matter* 22:265005.
65. Fonari A, Stauffer S (2013) vasp_raman_py. Version 0.5.1. Available at https://github.com/raman-sc/VASP/. Accessed January 3, 2019.